Knee of the cosmic hydrogen and helium spectrum below 1 PeV measured by ARGO-YBJ and a Cherenkov telescope of LHAASO

B. Bartoli,[2,3,‡] P. Bernardini,[4,5,‡] X. J. Bi,[1,‡] Z. Cao,[1,†,‡] S. Catalanotti,[2,3,‡] S. Z. Chen,[1,‡] T. L. Chen,[6,‡] S. W. Cui,[7,‡] B. Z Dai,[8,‡] A. D'Amone,[4,5,‡] Danzengluobu,[6,‡] I. De Mitri,[4,5,‡] B. D'Ettorre Piazzoli,[2,3,‡] T. Di Girolamo,[2,3,‡] G. Di Sciascio,[9,‡] C. F. Feng,[10,‡] Zhaoyang Feng,[1,‡] Zhenyong Feng,[11,‡] Q. B. Guo,[1,‡] Y. Q. Guo,[1,‡] H. H. He,[1,‡] Haibing Hu,[6,‡] Hongbo Hu,[1,‡] M. Iacovacci,[2,3,‡] R. Iuppa,[9,12,‡] H. Y. Jia,[11,‡] Labaciren,[6,‡] H. J. Li,[6,‡] C. Liu,[1,‡] J. Liu,[8,‡] M. Y. Liu,[6,‡] H. Lu,[1,‡] L. L. Ma,[1,‡] X. H. Ma,[1,‡] G. Mancarella,[4,5,‡] S. M. Mari,[13,14,‡] G. Marsella,[4,5,‡] S. Mastroianni,[3,‡] P. Montini,[9,‡] C. C. Ning,[6,‡] L. Perrone,[4,5,‡] P. Pistilli,[13,14,‡] P. Salvini,[15,‡] R. Santonico,[9,12,‡] P. R. Shen,[1,‡] X. D. Sheng,[1,‡] F. Shi,[1,‡] A. Surdo,[5,‡] Y. H. Tan,[1,‡] P. Vallania,[16,17,‡] S. Vernetto,[16,17,‡] C. Vigorito,[17,18,‡] H. Wang,[1,‡] C. Y. Wu,[1,‡] H. R. Wu,[1,‡] L. Xue,[10,‡] Q. Y. Yang,[8,‡] X. C. Yang,[8,‡] Z. G. Yao,[1,‡] A. F. Yuan,[6,‡] M. Zha,[1,‡] H. M. Zhang,[1,‡] L. Zhang,[8,‡] X. Y. Zhang,[10,‡] Y. Zhang,[1,‡] J. Zhao,[1,‡] Zhaxiciren,[6,‡] Zhaxisangzhu,[6,‡] X. X. Zhou,[11,‡] F. R. Zhu,[11,‡] Q. Q. Zhu,[1,‡] Y. X. Bai,[1,§] M. J. Chen,[1,§] S. H. Feng,[1,§] B. Gao,[1,§] M. H. Gu,[1,§] C. Hou,[1,§] J. Liu,[1,§] J. L. Liu,[19,§] X. Wang,[10,§] G. Xiao,[1,§] B. K. Zhang,[20,§] S. S. Zhang,[1,*,§] B. Zhou,[1,§] and X. Zuo[1,§]

(ARGO-YBJ Collaboration)‡

(LHAASO Collaboration)§

[1]*Key Laboratory of Particle Astrophysics, Institute of High Energy Physics, Chinese Academy of Sciences, 100049 Beijing, China*
[2]*Dipartimento di Fisica dell'Università di Napoli "Federico II", Complesso Universitario di Monte Sant'Angelo, via Cinthia, 80126 Napoli, Italy*
[3]*Istituto Nazionale di Fisica Nucleare, Sezione di Napoli, Complesso Universitario di Monte Sant'Angelo, via Cinthia, 80126 Napoli, Italy*
[4]*Dipartimento di Matematica e Fisica "Ennio De Giorgi" Università del Salento, via per Arnesano, 73100 Lecce, Italy*
[5]*Istituto Nazionale di Fisica Nucleare, Sezione di Lecce, via per Arnesano, 73100 Lecce, Italy*
[6]*Tibet University, 850000 Lhasa, Xizang, China*
[7]*Hebei Normal University, 050016 Shijiazhuang, Hebei, China*
[8]*Yunnan University, 2 North Cuihu Rd., 650091 Kunming, Yunnan, China*
[9]*Istituto Nazionale di Fisica Nucleare, Sezione di Roma Tor Vergata, via della Ricerca Scientifica 1, 00133 Roma, Italy*
[10]*Shandong University, 250100 Jinan, Shandong, China*
[11]*Southwest Jiaotong University, 610031 Chengdu, Sichuan, China*
[12]*Dipartimento di Fisica dell'Università di Roma "Tor Vergata" via della Ricerca Scientifica 1, 00133 Roma, Italy*
[13]*Dipartimento di Fisica dell'Università "Roma Tre", via della Vasca Navale 84, 00146 Roma, Italy*
[14]*Istituto Nazionale di Fisica Nucleare, Sezione di Roma Tre, via della Vasca Navale 84, 00146 Roma, Italy*
[15]*Istituto Nazionale di Fisica Nucleare, Sezione di Pavia, via Bassi 6, 27100 Pavia, Italy*
[16]*Osservatorio Astrofisico di Torino dell'Istituto Nazionale di Astrofisica, via P. Giuria 1, 10125 Torino, Italy*
[17]*Istituto Nazionale di Fisica Nucleare, Sezione di Torino, via P. Giuria 1, 10125 Torino, Italy*
[18]*Dipartimento di Fisica dell'Università di Torino, via P. Giuria 1, 10125 Torino, Italy*
[19]*Physics Department, Kunming University, 650214 Kunming, Yunnan, China*
[20]*Normal College of Fuyang, Fuyang 236029, China*

(Received 3 February 2015; published 6 November 2015)

The measurement of the cosmic ray energy spectrum, in particular for individual species of nuclei, is an important tool to investigate cosmic ray production and propagation mechanisms. The determination of the "knees" in the spectra of different species remains one of the main challenges in cosmic ray physics. In fact, experimental results are still conflicting. In this paper we report a measurement of the mixed proton and helium energy spectrum, obtained with the combined data of the ARGO-YBJ experiment and a wide field of view Cherenkov telescope, a prototype of the future LHAASO experiment. By means of a multiparameter technique, we have selected a high-purity proton plus helium sample. The reconstructed energy resolution is found to be about 25% throughout the investigated energy range from 100 TeV to 3 PeV, with a systematic uncertainty in the absolute energy scale of 9.7%. The found energy spectrum can be fitted with a broken power-law function, with a break at the energy $E_k = 700 \pm 230(\text{stat}) \pm 70(\text{sys})$ TeV, where the spectral

*zhangss@ihep.ac.cn
†caozh@ihep.ac.cn

index changes from -2.56 ± 0.05 to -3.24 ± 0.36. The statistical significance of the observed spectral break is 4.2 standard deviations.

DOI: 10.1103/PhysRevD.92.092005 PACS numbers: 96.50.sb, 96.50.sd, 98.70.Sa

I. INTRODUCTION

Galactic cosmic rays are believed to originate from astrophysical sources, such as supernova remnants. Several acceleration mechanisms have been proposed to describe the observed power-law behavior of their energy spectrum [1], but the identification of sources able to accelerate particles up to PeV energies and beyond is still one of the main open problems of high-energy astrophysics. A handful of significant structures in the cosmic ray spectrum has been observed, the most important being the so-called "knee," a clear steepening around 3×10^{15} eV [2,3]. The knee is believed to be a strong constraint for acceleration and propagation models. In one scenario, for example, the knee represents the highest energy that the Galactic cosmic ray sources can reach in accelerating particles [4,5]. The spectrum of all cosmic rays, however, does not appear to bend sharply, suggesting that different species may have different cutoff energies and that the flux may have contributions from extragalactic sources, expected to dominate the flux at energies above 10^{17}–10^{18} eV [6]. Unfortunately, a straightforward investigation of the spectral features has been very difficult in the past, mainly due to the following experimental limitations: (1) Direct measurements of cosmic ray spectra for specific nuclear species performed by space or balloon-borne detectors are constrained by their small exposures due to limited payloads, so that statistically reliable measurements cannot effectively extend to an energy higher than 10^{14} eV [7,8], which is far below the knee. (2) Ground-based experiments detecting extensive air showers (EAS) are affected by large uncertainties in the primary particle energy reconstruction and lack of effective methods to determine the mass of primary particles [9,10]. In EAS experiments, both energy and mass reconstructions largely rely on model-dependent shower simulations. As a consequence, mainly because of the unknown cosmic ray composition and imprecise energy calibrations, the position of the knee of the cosmic ray spectrum ranges between 1 and 6 PeV according to the different experiments, as summarized in Ref. [2] and in Fig. 1 of Ref. [11]. The uncertainty in the measurement of the pure proton spectrum is still large, e.g. the proton knee is found at several hundreds TeV by CASA-MIA [12] and at a few PeVs by KASCADE [10]. The lack of a precise evaluation of the knee energy for individual species prevents a fruitful developement of well-founded theories on the origin of cosmic rays.

The situation has improved with the data of the ARGO-YBJ experiment. ARGO-YBJ is an EAS detector made of a continuous array of resistive plate chambers (RPC), operated at 4300 m above sea level in Tibet [13]. The capability to record almost every secondary charged particle of showers incident on the RPC carpet, brings down the energy range studied by ARGO-YBJ to overlap that of CREAM [7], allowing a cross-check with direct measurements up to energies of ~100 TeV. With the measurement of the displacement of the Moon shadow under the effect of the geomagnetic field, ARGO-YBJ can calibrate the absolute energy scale up to 30 TeV [14]. Selecting light primaries according to the lateral distribution of secondary particles near the shower core, ARGO-YBJ performed a measurement of the hydrogen plus helium (H&He) spectrum between 3 and 300 TeV, with a systematic uncertainty less than 10% [15,16].

Using a multiparametric analysis, the combined detection of showers with both ARGO-YBJ and a wide field of view Cherenkov telescope (WFCT) [17] further improves the resolution of reconstructed energy and the separation of showers induced by H&He from those initiated by heavier nuclei [18]. In this paper we describe the analysis of the coincident events recorded by ARGO-YBJ and the WFCT and report the observation of a kneelike feature at 700 ± 230 TeV in the cosmic H&He spectrum. The hybrid experiment, data and simulations are described in Secs. II and III. The procedure of the primary energy reconstruction and the selection of a high-purity sample of proton and He events are described in Secs. IV and V. The final H&He energy spectrum is presented in Sec. VI. In Sec. VII we discuss the possible sources of systematic errors that affect both the measurements of the H&He flux and the primary energy. Further discussions and conclusions are given in Secs. VIII.

II. THE HYBRID EXPERIMENT

The data used in this work were collected simultaneously by ARGO-YBJ and a single wide field of view Cherenkov telescope located at the Yangbajing Cosmic Ray Observatory (Tibet, 4300 m asl, 606 g/cm^2). The Cherenkov telescope is located 79 m away the center of the ARGO-YBJ central carpet in the southeast direction. The telescope (named WFCT-02) has been operated starting from 2008. Another similar instrument (named WFCT-01) is 99 m off the center of the ARGO-YBJ carpet in the northwest direction. Both WFCT-01 and WFCT-02 are the prototypes of the future telescopes of the LHAASO experiment [19,20].

Each Cherenkov telescope [17] consists of an array of 16×16 Photonis XP3062 photomultipliers (PMTs) and a

4.7 m^2 spherical aluminized mirror. It has a field of view (FOV) of $14° \times 16°$ with a pixel size of approximately $1° \times 1°$. The photomultiplier tube (PMT) signals are fed to preamplifiers through a DC coupling and digitized by 50-MHz flash analog-to-digital converters (FADCs). The telescope also measures the sky background light intensity using the DC coupled PMT signals as a baseline. The telescope unit together with the power supply and a slow control system are installed in a 2.5 m × 2.3 m × 3 m shipping container. A glass window is installed at the entrance aperture to prevent dust from entering the apparatus. The main optical axis of the telescope has an elevation of 60° and observes showers within an angle of about 30° from the zenith. A simple majority trigger (SMT) was used for the science data collection that requires at least three adjacent PMTs above a threshold of 30 photoelectrons (PEs) within 160 ns. The shower image records the accumulated Cherenkov photons produced in the shower development. In our simulation and data analysis the PMT photocathode spectral response curve from the PMT data sheet [21] was used. A UV LED (375 nm) mounted at the center of the mirror, together with two pre-calibrated PMTs on the focal plane (two XP3062 PMTs, same as the ones used in the WFCT, were calibrated at the HiRes laboratory with a hybrid photo diode that was calibrated at US NIST. See [17] for more details.), was used to calibrate the gain of all 256 Photonics PMTs and monitor their stability during the data collection. The systematic uncertainty of the calibration is about 7% [17]. The PMTs were operated at a gain of 2×10^5, covering a linear dynamic range between 10 PEs and 3.2×10^4 PEs. As described below, the total number of photoelectrons in the Cherenkov image is used to reconstruct the shower energy. The shape of the shower image recorded by the PMT array was used to select the high-purity proton and helium-induced showers.

The ARGO-YBJ detector [13] includes a central RPC carpet of $\sim 78 \times 74$ m^2 with ~93% active area, formed with 130 clusters, and 23 guard-ring clusters covering up to $\sim 110 \times 100$ m^2. Each cluster (5.7×7.6 m^2) is made of 12 RPCs, and each RPC (1.25×2.8 m^2) is divided into 10 pads, which are read out by eight strips. Each strip represents the space granularity of the detector. Signal from each pad is sent to a time-to-digital converter (TDC) and represents the time pixel with a time resolution of about 1.8 ns [22]. The number of fired pads in the central carpet greater than 20 pads in a time window of 420 ns implements the inclusive trigger that starts the DAQ. The corresponding trigger rate is ~3.5 kHz. Data from the RPC, which has a maximum density of 23 strips/m^2, are used to study the primary spectrum below a few hundred TeV [15,16]. To enlarge the dynamic range up to PeV energies, each chamber is equipped with two analog readout "Big Pads" (1.39×1.23 m^2) which collect the total charge induced by particles passing through the chamber [23,24]. The collected charge is calibrated to be proportional to the number of charged particles [24–26]. The analog readout of the ARGO-YBJ RPC detector allows for a very detailed and precise measurement of the number of charged particles around the shower core induced by cosmic ray primary particles with energy higher than 100 TeV. Four full scale dynamic gains were adopted in different time periods in the analog readout system in order to effectively cover the primary cosmic ray energy up to several PeV. The full scale gains of 0.29, 2.13, 16.2, and 32.4 V have been used between December 2009 and June 2010, between July 2010 and August 2010, between August 2010 and July 2012, and after July 2012, respectively. The central carpet contains 3120 Big Pads, with only 3% of all channels not functioning properly. Two calibration methods, the iso-gradient method [25] and a method based on the direct comparison between analog and digital measurements [24], are applied to calibrate the gain of the Big Pads. The difference between the two calibrations is ~3.7% [25]. The gain of the Big Pads is determined with an uncertainty of about $(2.3\%)_{\rm stat} + (3.5\%)_{\rm sys}$ in the single data acquisition runs. Its mean time derivative is found to be +4.3%/year [24], indicating the detector stability. The slight decrease of the signal charge, observed in the last three years of operations, does not affect the digital readout and the trigger efficiency. More details of the analog readout performance can be found in previous reports [24,25]. According to Monte Carlo (MC) simulations, the largest number of particles $N_{\rm max}$ recorded by an RPC in a given shower is a useful parameter to measure the particle density in the shower core region, i.e. within 5 m from the core position. For a given energy, $N_{\rm max}$ is found to be smaller in showers induced by heavy nuclei than that in showers induced by light nuclei. Therefore, in this work $N_{\rm max}$ will be used to select different primary masses.

III. DATA AND SIMULATION

The EAS events that triggered both the WFCT-02 and ARGO-YBJ detectors between December 2010 and February 2012 are used for the analysis presented in this paper. The coincidence events are selected by an off-line matching of the GPS time stamp of events recorded by the two detectors. A time window of 8 μs containing a WFCT-02 event is searched for coincidence in the ARGO-YBJ detector event stream. The Cherenkov telescope recorded data in moon-less nights. Constraints on the exposure of the hybrid experiment are given by weather and atmosphere conditions, which were monitored by using the bright stars in the FOV of the telescope and an infrared camera covering the whole sky. More details about the criteria for the observational conditions can be found elsewhere [18,27]. Under satisfactory weather and atmosphere conditions, a total exposure time of 7.28×10^5 seconds was obtained between December 2010 and February 2012, when the RPC array was also taking data.

We selected well-reconstructed showers in the effective aperture of the ARGO-YBJ/WFCT hybrid system according to the following criteria: (1) well-reconstructed shower core position contained in the ARGO-YBJ central carpet, excluding an outer region by 1 meter, (2) space angle between the incident direction of the shower and the telescope main axis less than 6°, (3) more than 1000 fired pads on the ARGO-YBJ central carpet, and (4) more than six fired pixels in the WFCT-02 PMT matrix. About 32,700 events survived this selection. Among them, 8218 showers have a reconstructed primary energy above 100 TeV. We checked the possible saturation effects in both RPC and WFCT-02 PMTs for all the selected events. All $N_{\max}$ values were found to be less than 2×10^4 particles, which is the saturation point of Big Pads (see Fig. 24 of Ref. [24]). For the events up to 3 PeV presented in this work, all telescope PMT channels showed less than 3.2×10^4 PEs, the upper limit of the PMT dynamic range. These cuts also garantee that the Cherenkov images of the selected events are fully contained in the FOV. The angular resolution for the coincident events is about 0.3° and the shower core position resolution about 2 m, according to the ARGO-YBJ reconstruction [28]. The shower direction and the core location reconstructed by ARGO-YBJ were used to determine the impact parameter, a fundamental parameter in the analysis of the Cherenkov data. For the selected showers, according to the MC simulation, the hybrid measurement above 100 TeV has a nearly constant aperture with energy, equal to 163 m^2 sr (see the all-particle aperture in Fig. 7 below).

Extensive air showers, including the Cherenkov emission, were simulated with the CORSIKA [29] package, where high-energy hadronic interactions were simulated by QGSJETII-03 [30] and low-energy processes by GHEISHA [31]. The G4argo [32] package and a ray-tracing procedure on the Cherenkov photons [33] were applied for the simulation of the detector responses. Showers initiated by five mass groups including proton, helium, C-N-O group, Mg-Al-Si group and iron were generated in the simulation. The configuration of all the materials in the ARGO-YBJ experimental hall, the performance of the RPC array, and the performance of the digital readout and analog readout of the RPCs were included in the ARGO-YBJ detector simulation. The detailed structure of the shipping container, the PMT quantum efficiency, the characteristics of the mirror and the glass windows, and finally the electronic readout system were included in the Cherenkov telescope simulation. The comparison between the simulation and data was made for the distribution of the total number of photoelectrons in Cherenkov images, the distribution of shower zenith angles and impact parameters. The agreement was satisfactory, with a $\chi^2/\text{n.d.f} = 1.6, 1.7, 1.5$ for these three distributions, respectively [18]. The composition and spectral model by Hörandel [34], in the energy range from 10 TeV to 10 PeV, was used in this comparison.

IV. SHOWER ENERGY RECONSTRUCTION AND N_{pe} DISTRIBUTION FOR ALL-PARTICLE SPECTRUM

The shower energy is reconstructed from the total number of photoelectrons N_{pe} recorded by the Cherenkov telescope. One advantage of using air Cherenkov photons instead of charged secondary particles in showers is that Cherenkov photons have much larger attenuation length in the atmosphere than the radiation length of charged particles. Therefore, a large amount of the Cherenkov photons produced during the entire shower development can be accumulated on the light collector of the Cherenkov telescope. On the other hand, the number of photoelectrons drops fast increasing the impact parameter R_p due to geometric effects. An example is shown in Fig. 1 for proton showers of different energies. Because of the shielding due to the walls of the container, the effective area of the mirror also depends on the space angle between the EAS incident direction and the Cherenkov telescope main axis, denoted as α. Using a very large sample generated by the simulation described above, look-up tables for the shower energy with three parameters, i.e., N_{pe}, R_p and α, were produced for different mass groups. For a shower with N_{pe} measured by the telescope and R_p and α determined using the RPC array, the primary energy can be read out from these tables by assuming a mass group for the primary particle. The distribution of the difference between the reconstructed energy and the true one is found to be symmetric and can be described with a Gaussian function, regardless of the mass group assumptions. Using the look-up table made for proton and helium primaries, the standard deviation σ of the reconstructed energy for all particles (i.e. five groups of proton, helium, C-N-O, Mg-Al-Si, and iron) is 27%, and decreases to 23% when the look-up table is

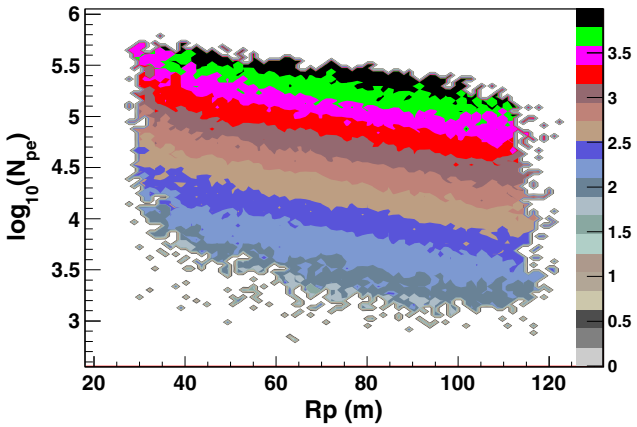

FIG. 1 (color online). The total number of photoelectrons N_{pe} as a function of the impact parameter R_p for primary protons. The color scale represents the shower energies in bins of $\Delta\log_{10}(E/1\ \text{TeV}) = 0.2$, covering primary energies from 30 TeV to 10 PeV.

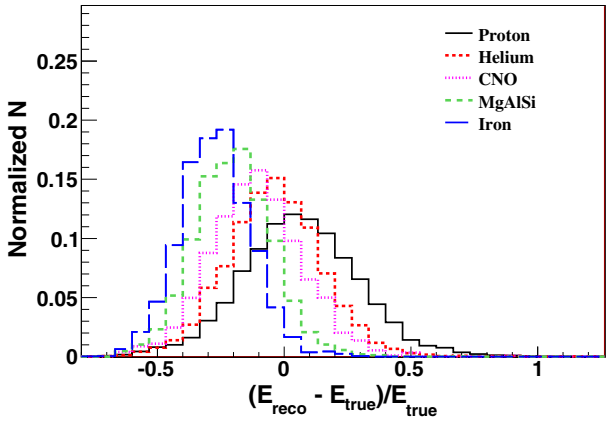

FIG. 2 (color online). The simulated distribution of $(E_{\rm true} - E_{\rm reco})/E_{\rm true}$ for different mass groups in the energy range 500–800 TeV. The reconstructed energy is obtained from the look-up table built for primaries p + He in 1:1 ratio.

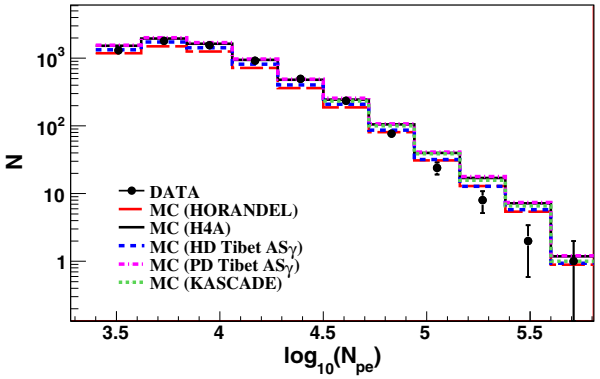

FIG. 3 (color online). Distribution of the number of Cherenkov photoelectrons (N_{pe}) measured by the telescope (filled circles). The histograms represent the N_{pe} distributions obtained by simulations according to the flux models [34,36] and to the all-particle spectra and corresponding composition models reported by the Tibet AS$_\gamma$ [35] and KASCADE[10] experiments. The bin size is 0.22 in $\log_{10}N_{pe}$.

made for heavier primaries. The primary energy determined in this way shows a systematic shift that depends on the nature of the primary. For example, the difference between the mean energy of proton and iron showers is approximately 37% as shown in Fig. 2, greater than the standard deviation. This means, for a mixed primary composition, that a correct all-particle energy spectrum could be obtained only if the composition could be determined *a priori* and the corresponding look-up table is used.

For this, in order to compare the energy distribution of our events with the ones obtained by other experiments or with existing models, we prefer to use the variable N_{pe} instead of the energy, avoiding the full energy reconstruction that requires a specific mixture of primary masses to choose the proper look-up table. Since the N_{pe} is an observable that does not depend on composition assumptions, we compared the N_{pe} distribution of our data with those obtained simulating different all-particle spectra. Figure 3 shows the experimental distribution of N_{pe}, compared with the distribution of simulated N_{pe} obtained by using as input spectra the all-particle spectra from the Tibet AS$_\gamma$ [35] and KASCADE [10] experiments and the corresponding composition models. The N_{pe} distributions obtained assuming the composition models of Hörandel [34] and H4a [36] are also shown in the same figure. The comparison covers an energy range from 126 TeV to 15.8 PeV, according to the conversion N_{pe} energy given by the look-up table made for 1:1 proton and helium primaries. An overall agreement is found at a level of 30%.

V. HYDROGEN AND HELIUM EVENT SELECTION

The secondary particles in showers induced by heavy primaries are spread further away from the core region than light primaries. Therefore, difference exists in the secondary particle distribution near the core between showers induced by light and heavy nuclei [26]. Beyond a certain distance, e.g., 20 m from the core, the lateral distributions become similar because they are mainly affected by multiple Coulomb scattering of the secondary particles and can be well described by the Nishimura-Kamata-Greisen (NKG) function. With its full coverage, the ARGO-YBJ array precisely measures the lateral distribution of the secondary particle density in the shower core region. The number of particles recorded by the most hit RPC in an event, denoted as $N_{\rm max}$, is a good parameter to discriminate between showers with different lateral distribution within 3 m from the cores. In a shower induced by a heavy nucleus, $N_{\rm max}$ is expected to be smaller than that in a shower induced by a light nucleus with the same energy [26]. Obviously, for a give primary mass, $N_{\rm max}$ also depends on the energy. We found from simulations that $N_{\rm max}$ is proportional to $(N_0^{pe})^{1.44}$ where N_0^{pe} is the total number of photoelectrons normalized to $R_p = 0$ and $\alpha = 0°$ (see Fig. 4). We define a reduced dimensionless variable $p_L = \log_{10}N_{\rm max} - 1.44\log_{10}N_0^{pe}$ to describe the $N_{\rm max}$ and N_0^{pe} correlation.

The shape of the shower image recorded by the Cherenkov telescope is also a mass-sensitive parameter. The elliptical characteristics are described by the Hillas parameters [37], width and length. Generally, the Cherenkov image is more stretched, i.e., narrower and longer, for showers that are more deeply developed in the atmosphere. For a given energy and impact parameter, the length to width ratio (L/W) is a parameter sensitive to the depth of the shower maximum, that is related to the nature of the primary. It is also known that the images are more elongated for showers at larger distance from the telescope because of geometric effects. The ratio L/W is nearly proportional to the shower impact parameter R_p (Fig. 5), but in our case depends weakly on the shower size

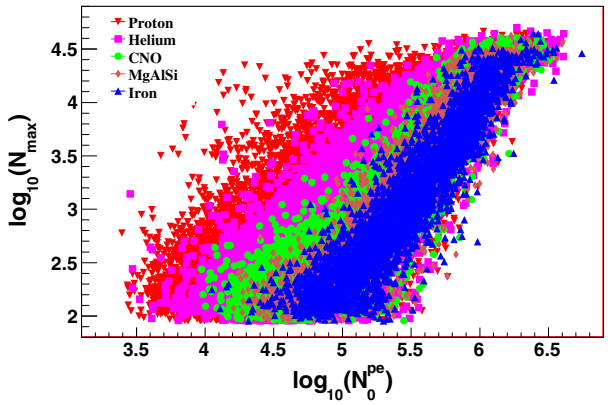

FIG. 4 (color online). The simulated largest number of particles in the RPC ($N_{\max}$) as a function of the simulated number of photoelectrons in the Cherenkov telescope (N_0^{pe}, normalized to $R_p = 0$ and $\alpha = 0°$). The separation between the different mass groups is visible.

measured by N_0^{pe}. By a series of MC studies, we have introduced a reduced dimensionless variable $p_C = L/W - R_p/109.9\ \mathrm{m} - 0.1\log_{10}N_0^{pe}$ that takes into account the L/W correlation with both R_p and N_0^{pe}.

The H&He sample for this work was selected from the coincident events by combining the two composition-sensitive parameters p_L and p_C. MC studies show that different composition groups can be statistically separated on the p_L-p_C map [18]. A contour plot of the map for two mass groups, H&He and all other nuclei (C-N-O, Mg-Al-Si and iron) in the energy range between 100 TeV and 10 PeV, is shown in Fig. 6. The cuts $p_L \geq -4.53$ or $p_C \geq 0.78$ result in a selected sample of H&He showers with a purity of 93% below 700 TeV and an efficiency of 72% assuming the Hörandel composition models [34]. The aperture, defined as the geometrical aperture (163 $\mathrm{m}^2\,\mathrm{sr}$) times the

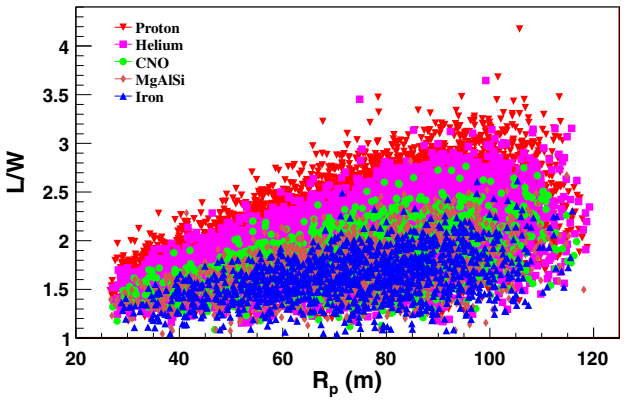

FIG. 5 (color online). The length to width ratio (L/W) of the shower Cherenkov image as a function of the impact parameter R_p, for showers with $\log_{10}N_0^{pe}$ between 5.0 and 5.3, according to simulations. The separation between the different mass groups is visible.

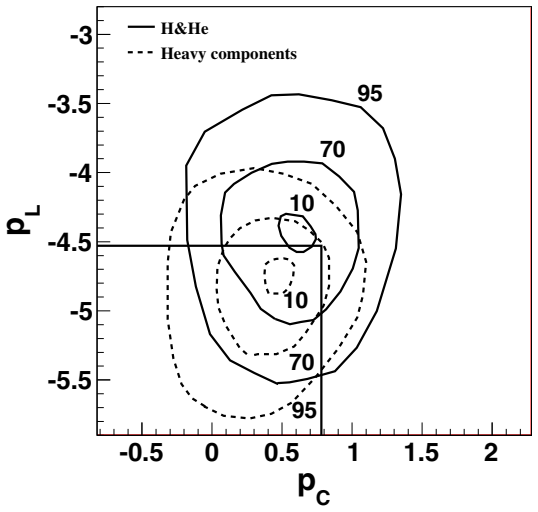

FIG. 6 (color online). Composition-sensitive parameters p_L and p_C for two mass groups, H&He (solid contours) and heavier masses (dashed contours) including 1:1:1 mixing of CNO, MgAlSi, and iron. The primary energy of the plotted events is between 100 TeV and 10 PeV. Numbers on the contours indicate the percentage of contained events.

selection efficiency, gradually increases to 120 $\mathrm{m}^2\,\mathrm{sr}$ at 300 TeV and remains nearly constant at higher energies (see Fig. 7). The selection efficiency is defined as the ratio of the selected number of H&He events and the total number of injected H&He events in the simulation. In the selected sample, the contamination from the heavy nuclei increases with primary energy and depends on the composition. Assuming the Hörandel composition [34], the contamination of heavy species is found to be 13% at energies around 1 PeV, and gradually increases to 27% around 3 PeV, which is shown in Fig. 8. The contamination fraction for different mass groups in Fig. 8 is defined as $N_i/(N_{\mathrm{H}} + N_{\mathrm{He}} + N_{\mathrm{CNO}} + N_{\mathrm{MgAlSi}} + N_{\mathrm{iron}})$ with $N_i = N_{\mathrm{CNO}}$, N_{MgAlSi}, N_{iron}

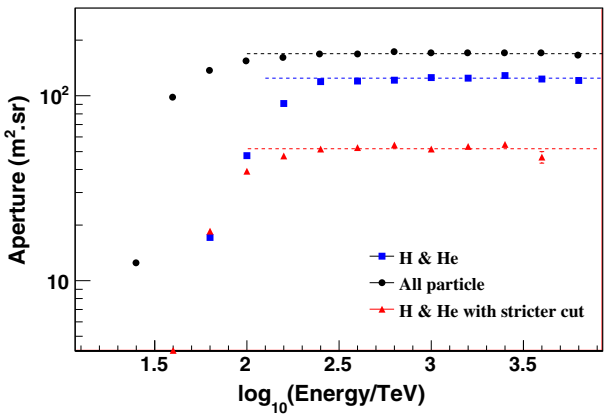

FIG. 7 (color online). Aperture of the hybrid experiment. Solid circles represent the aperture for all particles, solid squares for the selected H&He events, triangles for the H&He events obtained with stricter cuts for calibration purposes using the low-energy part of the spectrum [18].

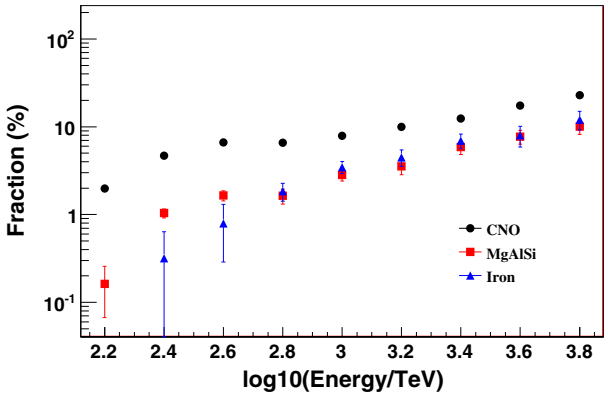

FIG. 8 (color online). The contamination fraction (%) of events of different heavy composition groups that survive through the H&He selection cuts. The Hörandel model is assumed in the simulation.

for $i = 1, 2, 3$. The associated uncertainty on the light component flux is discussed below.

For the selected H&He events, their energies are better defined because the intrinsic difference between H and He showers of the same energy is smaller than 10% in our detectors, which is significantly lower than the energy resolution. About 40,000 simulated events that survived all the reconstruction quality cuts and the H&He selection procedure were used to derive the resolution of the reconstructed energy. We compared the reconstructed energy $E_{\rm reco}$ and the true energy $E_{\rm true}$ in the MC simulation. The distributions of the $\Delta E = E_{\rm reco} - E_{\rm true}$ at 300 TeV, 1 PeV and 3 PeV are shown in Fig. 9. The energy resolution is about 25%, nearly constant, with an offset less than 3% throughout the energy range up to 3 PeV (Table I). This helps to achieve a minimal distortion of the spectrum in the interested energy range.

VI. ENERGY SPECTRUM OF PROTON AND HELIUM

The flux of H&He is calculated by

$$J(E) = \frac{\Delta N^{\rm Measured}_{\rm H\&He}}{\Delta E \cdot T \cdot A_{\rm H\&He}} = \frac{\Delta N_{\rm H\&He} + \Delta N_{\rm Heavy}}{\Delta E \cdot T \cdot A_{\rm H\&He}}, \quad (1)$$

where $\Delta N^{\rm Measured}_{\rm H\&He}$ is the measured number of H&He-like events in an energy bin (ΔE). $\Delta N^{\rm Measured}_{\rm H\&He}$ has two parts, $\Delta N_{\rm H\&He}$ (the number of pure H&He events) and $\Delta N_{\rm Heavy}$ (the number of heavy contamination events) in each energy bin. T is the total exposure time for the used data. $A_{\rm H\&He}$ is the aperture of the hybrid detection system for pure H&He component.

Following the H&He selection and energy reconstruction procedures described, respectively, in Secs. V and IV, we have obtained the energy spectrum of the H&He component shown in Fig. 10. The number of events in each energy bin and the corresponding detector aperture are shown in Table I. The bin width is chosen to be 0.2 in $\log_{10}(E/1\ {\rm TeV})$, corresponding to the resolution listed in the sixth row of Table I. To take into account the energy resolution and possible smearinglike bin-to-bin migration between the true and reconstructed primary energies, a Bayesian algorithm [39] was applied to unfold the reconstructed events. The selection efficiency for He showers is about 80% of that for H showers. The observed spectrum can be successfully fitted with a broken power-law function

$$J(E) = \begin{cases} J(E_k) \cdot (E/E_k)^{\beta_1} & (E < E_k) \\ J(E_k) \cdot (E/E_k)^{\beta_2} & (E > E_k) \end{cases} \quad (2)$$

with $E_k = 700 \pm 230$ TeV, $J(E_k) = (4.65 \pm 0.27) \times 10^{-12}\,{\rm GeV^{-1}\,m^{-2}\,s^{-1}\,sr^{-1}}$, $\beta_1 = -2.56 \pm 0.05$ and $\beta_2 = -3.24 \pm 0.36$. The relatively large error on the breaking energy E_k is due to the limited statistics. Considering a systematic uncertainty in the absolute energy scale of 9.7% (see the next session for a more detailed discussion), the systematic uncertainty in E_k is estimated to be ~70 TeV.

We previously reported a similar analysis with tighter cuts for light component selection to obtain a H&He sample with higher purity (98% assuming the composition models given in [34]) for events below 700 TeV [18]. The aperture in that analysis was much smaller (~50 m^2 sr, as shown in Fig. 7) and the selection efficiency was around 30%. The H&He spectrum that we previously obtained was consistent with a single-index power law, in good agreement with CREAM [7] and ARGO-YBJ [15,16] results (see Fig. 10). The overall difference between our flux and

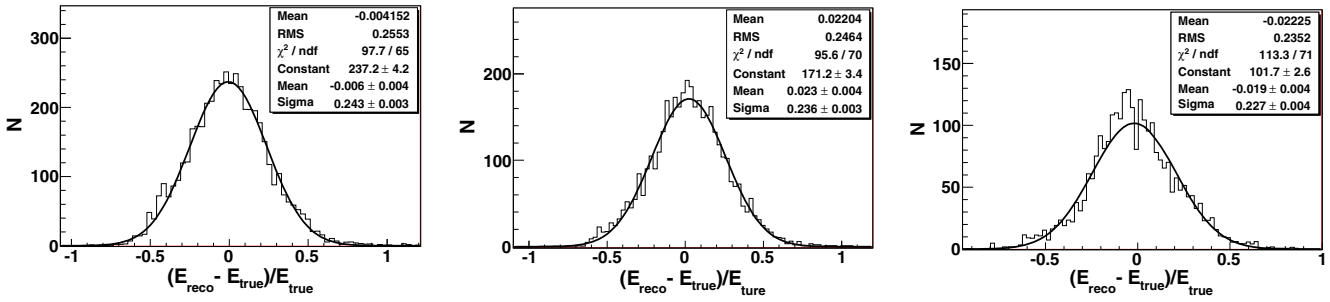

FIG. 9 (color online). The energy resolution at ~300 TeV (left), ~1 PeV (middle) and ~3 PeV (right) for a H&He sample. The distributions are fitted with a Gaussian function.

TABLE I. Relevant data related to the H&He spectrum evaluation. For each energy bin of the spectrum, the table reports (1) the logarithm of the energy, (2) the number of H&He-like events, (3) the measured flux, (4) the aperture, (5) the energy resolution, (6) the energy offset in the energy reconstruction, (7) the number of contaminating heavy nuclei evaluated under the assumptions given in the text.

$\log_{10}(E_{\rm min}/1\ {\rm TeV})$-$\log_{10}(E_{\rm max}/1\ {\rm TeV})$	2.1–2.3	2.3–2.5	2.5–2.7	2.7–2.9	2.9–3.1	3.1–3.3	3.3–3.5
$\log_{10}(E_{\rm center}/1\ {\rm TeV})$	2.2	2.4	2.6	2.8	3.0	3.2	3.4
Number of events	1030	640	339	156	64	21	9
$10^{12}\times{\rm Flux}({\rm GeV}^{-1}\,{\rm m}^{-2}\,{\rm s}^{-1}\,{\rm sr}^{-1})$	212.1 ± 6.6	63.1 ± 2.5	20.9 ± 1.1	6.01 ± 0.48	1.51 ± 0.19	0.315 ± 0.069	0.083 ± 0.028
Aperture (m^2 sr)	90.6	119.4	120.3	121.7	125.7	124.5	128.5
Energy resolution	26.2%	25.7%	24.9%	25.1%	24.6%	24.2%	23.8%
Energy offset	−0.04%	−0.6%	−0.3%	1.9%	2.2%	1.0%	0.1%
Contaminating heavy nuclei	$20.1^{+6.0}_{-4.5}$	$39.2^{+5.5}_{-10.0}$	$28.2^{+2.5}_{-7.4}$	$13.7^{+1.0}_{-3.5}$	$9.4^{+1.4}_{-2.4}$	$5.3^{+1.4}_{-1.3}$	$3.4^{+1.2}_{-0.8}$

the other measurements was found to be less than 9%, which makes us confident on the hybrid observation and the new analysis techniques developed for the measurement of both the absolute flux and the primary energy.

In the current analysis we adopt the same technique described in [18] but with looser cuts, in order to have a larger statistics and reach higher energies. As a consequence, the selected event sample purity is reduced to 93% below 700 TeV assuming the same composition model. Since the contamination of heavy nuclei increases with energy (see Fig. 8), the heavy contaminant not only increases the observed H&He spectrum flux, but also changes the spectrum index. To estimate how much the heavy contaminants introduced by the looser selection cuts affect the spectrum shape and index, we tried to subtract them from the spectrum by using the composition model given in Ref. [34]. We simulated the number of heavy nuclei that passed the selection cuts for each energy bin. The result is reported in the last row of Table I. Fitting the spectrum after the subtraction of these events, we obtain $E_k = 770\pm200$ TeV, $J(E_k) = (3.25\pm0.22)\times10^{-12}$ GeV^{-1} m^{-2} s^{-1} sr^{-1}, $\beta_1 = -2.62\pm0.05$, and $\beta_2 = -3.58\pm0.50$. This value of β_1 is in excellent agreement with the spectral index -2.63 ± 0.06 in our previous report, and correspondingly consistent with the spectral indexes reported by CREAM [7] and ARGO-YBJ [15,16].

The statistical significance of the observed knee feature reported in Fig. 10 was estimated by comparing the number of events observed above the knee with the number of events expected by extending at PeV energies the spectrum measured below the knee. The number of expected events in the three energy bins above the knee is 82, 39 and 20, respectively. The difference between the observed number of events (see Table I) and the expectation from a single power-law spectrum corresponds to a deficit with a statistical significance of 4.2 standard deviations. To see if any artificial feature could have been produced in our

TABLE II. Summary of systematic uncertainties.

1. Systematic uncertainties in the absolute energy measurement:	
Weather/atmosphere conditions	±7.6%
Photometric calibration	±5.6%
Interaction models	±2.1%
Composition models	±1%
2. Systematic uncertainties on the H&He flux:	
The contamination of heavy nuclei[a]	$-(1.5\sim2.5)$%@158 TeV
	$-(29\sim51)$%@2.5 PeV
ARGO-YBJ RPC calibration	±7%
Interaction models	±4.2%
Boundary selection	±3%
H&He selection efficiencies	±3%
Saturation of RPCs	±0.03%

[a]Contamination of heavy nuclei is not constant with energy and is dependent on composition models. The composition models of Ref. [34], Ref. [36] and Ref. [38] are assumed to estimated the uncertainties.

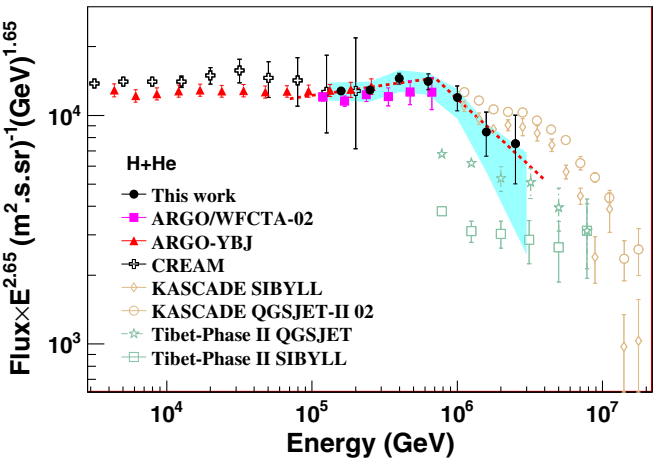

FIG. 10 (color online). H&He spectrum obtained by the hybrid experiment with ARGO-YBJ and the imaging Cherenkov telescope. A clear knee structure is observed around 700 TeV. The H&He spectra by CREAM [7], ARGO-YBJ [16] and the hybrid experiment [18] below the knee, the spectra by Tibet AS$_\gamma$ [9] and KASCADE [10] above the knee are shown for comparison. In our result, the error bar is the statistical error, and the shaded area represents the systematic uncertainty.

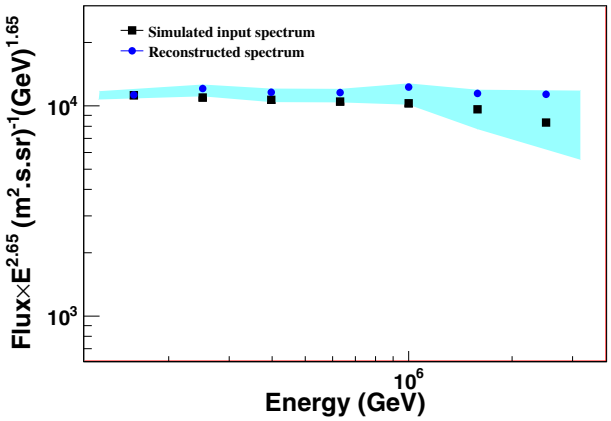

FIG. 11 (color online). Comparison between the input H&He spectrum according to Ref. [34] and the reconstructed one. The slightly harder reconstructed spectrum shape is consistent with the contamination from heavier components shown in Fig. 8. The shaded area represents the systematic uncertainty caused by the contamination of heavy nuclei and boundary selection.

analysis, we also conducted a dedicated simulation according to the composition model given in Ref. [34] that includes five different mass groups. After applying the same MC data quality cuts and the selection procedure for H&He showers, we obtained the reconstructed spectrum. The comparison between the reconstructed spectrum and the input H&He spectrum is shown in Fig. 11. The shaded area represents the systematic uncertainty caused by the contamination of heavy nuclei and boundary selection, which is discussed in the next section. Both spectra agree with each other within the systematic uncertainty, with no new kneelike breaks in the reconstructed spectrum.

VII. SYSTEMATIC UNCERTAINTIES

Systematic uncertainties discussed below include the uncertainties in both the reported flux and shower event energy reconstruction. The systematic uncertainties in the shower energy reconstruction include the following:

(1) The uncertainty in the weather and atmosphere conditions is estimated by using the starlight in the Galactic plane recorded by the Cherenkov telescope. A variance of $<9.5\%$ in the light intensity is observed after the good weather condition cuts, which corresponds to an uncertainty of 7.6% in the absolute energy scale.

(2) The uncertainty caused by the photometric calibration. The photometric calibration itself has an uncertainty of 7%. It introduces about 5.6% uncertainty in the energy determination. More details about the photometric calibration can be found elsewhere [17].

(3) The uncertainty related to the interaction models assumed in the simulation. By considering the high-energy interaction models SIBYLL and QGSJET, the uncertainty is found to be about 1.0%. For the low-energy interaction models GHEISHA and FLUKA, this uncertainty is about 1.9%.

(4) The uncertainty associated with the composition assumptions in the simulation, which was estimated by using several available composition models including the Hörandel model [34], the H4a model [36], and the one in Ref. [38]. About 1% of systematic uncertainty exists in the reconstructed energy.

The main contributions to the uncertainty in the flux evaluation include the following:

(1) The contamination of heavy nuclei, which is most important source of uncertainty. This contamination cannot be unambiguously determined since it depends on the elemental composition of cosmic rays, that is unknown in the energy range considered here. The last row in Table I reports the expected numbers of contaminating heavy nuclei assuming the Hörandel composition model [34]. The contamination increases with energy, from about 2.5% of the measured H&He flux at 158 TeV to about 13% at 1 PeV. The errors reported in the table, associated with the number of contaminating events, indicate the variation in case different composition models are assumed, including those in Refs. [36] and [38]. Obviously, if the heavy components would be more abundant than what described by the existing models, the contamination could be proportionally larger.

(2) The interaction models in the MC simulations. The flux uncertainty is about 2.3% by considering the high-energy interaction models SIBYLL [40] and QGSJET, and about 3.5% by considering the low-energy interaction models GHEISHA and FLUKA [41].

(3) Boundary effects in the hybrid detector aperture calculation. The associated uncertainty is related to the resolution of EAS core and direction reconstruction. By comparing the boundary defined by the event quality cuts and the real geometrical boundary, we found that the flux contains an additional uncertainty of about 3%.

(4) The difference between the H and He selection efficiencies. In the flux calculation, we used the same selection procedure for both H and He showers, which results in an uncertainty of about 3% in the overall flux according to composition models being considered.

(5) The calibration that gives the observed number of particles measured in the RPCs. The systematic uncertainty in the particle measurement by using the iso-gradient method to calibrate the RPCs is 10.7%, which also includes the uncertainty from the RPCs long-term stability [25]. The difference between the iso-gradient method and the other

calibration method described in Ref. [24] is about 3.7%. A flux uncertainty of 7% is found by combining these two methods to evaluate the number of particles measured by the RPCs.

(6) The saturation in RPCs. Each Big Pad has a dynamic range up to $\sim 2 \times 10^4$ particles (see Fig. 24 of Ref. [24]). Using $N_{\max} = 2 \times 10^4$, we have $\log_{10} N_0^{pe} = 6.13$ for $p_L = \log_{10} N_{\max} - 1.44 \log_{10} N_0^{pe} = -4.53$ (-4.53 is the lower of the p_L parameter boundaries for the H&He selection). The events with $\log_{10} N_0^{pe} \geq 6.13$ are about 0.03% of total number of events in the energy range of $\log_{10}(E/1\ \text{Tev}) = 3.3$ to 3.5 according to our simulations. Because each RPC consists of two Big Pads, $N_{\max}$ is therefore always greater than the number of particles recorded by one Big Pad. Therefore, the effect of the saturation of Big Pads can be ignored in the H&He selection below 3 PeV.

Systematic uncertainties are summarized in Table II. The total systematic uncertainty on the reconstructed energy is 9.7%. The total systematic uncertainty on the flux is plotted as the shaded area in Fig. 10.

VIII. DISCUSSION AND CONCLUSIONS

In the standard scenario of the cosmic ray origin, supernova remnants (SNRs) are considered the main source of Galactic cosmic rays. If about 10% of the supernova kinetic energy is fed into cosmic rays, SNRs can easily account for the energy density of cosmic rays resident in the Galaxy. Diffuse acceleration processes inside SNRs can produce a power-law spectrum up to very high energies with a spectral index close to 2. Theoretical models predict a rigidity dependent spectrum, and the kneelike feature observed in the all-particle spectrum may correspond to the maximum rigidity to which the dominant population of sources can accelerate cosmic rays, or may be related to the leakage from our Galaxy. This interpretation is further supported by the LHC results which exclude any dramatic change in the features of the hadronic interaction at least up to 10^{17} eV [42]. Thus the determination of the shape of the energy spectrum of proton and helium primaries, the most abundant elements and the first ones to reach the maximum acceleration energy, is of special relevance to understand cosmic ray acceleration and propagation in the Galaxy. In the ARGO-YBJ/WFCTA-02 hybrid experiment proton and helium induced showers have been selected with high efficiency by means of two mass-discriminant parameters, namely the number of charged particles in the shower core and the shape of the Cherenkov light image. These parameters weakly depend on the hadronic models in the analysis. The data of the hybrid experiment show a clear steepening in the flux of these light elements starting at an energy of about 700 TeV. Even taking into account the systematic uncertainty affecting this result, the decreasing flux of the primary proton and helium nuclei at energies below 1 PeV implies that the knee of the all-particle energy spectrum is likely related to the steepening in the energy spectrum of heavier components.

Indications about such a low-energy knee for H&He spectrum have been previously reported or favored by other experiments, including the Tibet AS_γ [35], CASA-MIA [12], and MACRO [43]. Using a traditional emulsion chamber and the EAS array, Tibet AS_γ observed very steep single-index power-law spectra of protons and helium nuclei that extends to about 100 TeV at the lower energy end. CASA-MIA reported the light component (H&He) event distribution, which has a break, without discussing the shower detection efficiency though, the H&He selection efficiency correction, or a possible contamination from heavy components. This experiment also provides indirect evidence of a low-energy knee in the proton spectrum, namely a rigidity-dependent composition changing its trend below 1 PeV. Using underground muons information, MACRO experiment results imply the existence of a knee around 500 TeV.

On the other hand, it is very interesting to note that the multicomponent unfolding analysis of the KASCADE data attributes the knee of the all particle spectrum observed at about 3.5 PeV to a steepening in the flux of protons and helium nuclei, even if the inferred spectra may depend on the hadronic code used in the analysis (see Fig. 10). This result determines that the individual nuclear components of the primary cosmic rays fall off at a magnetic rigidity of about 3 PV. The spectral features observed by KASCADE-Grande at energies up to 10^{17} eV are currently interpreted in the framework of this rigidity scaling model. However, the issue of whether SNRs are able to accelerate protons up to a few PeV is still an open question.

Precise measurement of the knee position for different mass components is of great theoretical interests in the study of cosmic ray origin. For example, whether SNRs are able to accelerate protons up to a few PeV is still an open question. The original work of Lagage and Cesarsky [44] fixed at about 100 TV the maximum rigidity achievable in the stochastic shock acceleration at supernova blast waves expanding in an average interstellar medium. Several attempts have been undertaken to better model this process for a more efficient acceleration. Magnetic field amplification [45], oblique shocks [46], acceleration in red-giant or Wolf-Rayet star winds [47] or acceleration at the Galactic-wind termination shock [48] are among the proposed processes able to extend the maximum energy beyond the knee region. The result of the hybrid experiment may mitigate the problem of reaching very high energies in supernovae, but determines new constraints to the interpretation of the KASCADE-Grande results. This issue has been discussed in [38]. The authors find that, while the ARGO-YBJ/WFCTA-02 hybrid experiment result can be easily accounted for, it is difficult to reconcile the results o f both experiments in the framework of a model of type II SNRs expanding in the wind produced by the red

super-giant progenitor stars. While predictions of other models are needed for a more complete comparison, this analysis points out the problem of combining results from very different experiments. A new-generation very large array, such as the proposed LHAASO experiment [19,20], densely instrumented to measure many EAS observables, should be able to investigate with unprecedented accuracy the features of the all-particle spectrum and their chemical composition over a wide energy range from 10^{14} to 10^{17} eV.

In summary the joint operation of the ARGO-YBJ detector with a wide field-of-view imaging Cherenkov telescope allowed a detailed investigation of the energy range bridging the gap between the direct observations of CREAM and the ground-based KASCADE experiment. This hybrid experiment yields a clear evidence for a kneelike structure in the spectrum of light primaries (protons and helium nuclei) at about 700 TeV. The observation of the knee of the primary light component at such a low energy provides valuable inputs to justify and improve Galactic cosmic ray acceleration models.

ACKNOWLEDGMENTS

This work is supported in China by the Chinese Academy of Sciences (CAS) (0529110S13), the Key Laboratory of Particle Astrophysics, Institute of High Energy Physics, CAS, and in Italy by the Istituto Nazionale di Fisica Nucleare (INFN). The Knowledge Innovation Fund (H85451D0U2) of IHEP, China, Projects No. 11475190, No. 10975145 and No. 11075170 of NSFC also provide support to this study. We acknowledge the essential support of W. Y. Chen, G. Yang, X. F. Yuan, C. Y. Zhao, R. Assiro, B. Biondo, S. Bricola, F. Budano, A. Corvaglia, B. D'Aquino, R. Esposito, A. Innocente, A. Mangano, E. Pastori, C. Pinto, E. Reali, F. Taurino, and A. Zerbini. We also appreciate the discussions with Professor Xinhua Bai (SDSM&T) in the investigation of saturations and uncertainties and his valuable comments and proofreading of the manuscript.

[1] J. R. Hörandel, Astropart. Phys. **21**, 241 (2004).
[2] J. Blümer, R. Engel, and J. R. Hörandel, Prog. Part. Nucl. Phys. **63**, 293 (2009).
[3] G. Kulikov and G. Khristiansen, JETP **35**, 635 (1958).
[4] A. D. Erlykin and A. W. Wolfendale, J. Phys. G **23**, 979 (1997).
[5] E. G. Berezhko and H. J. Völk, Astrophys. J. **661**, L175 (2007).
[6] V. Berezinsky, A. Z. Gazizov, and S. I. Grigorieva, Phys. Rev. D **74**, 043005 (2006).
[7] Y. S. Yoon *et al.*, Astrophys. J. **728**, 122 (2011).
[8] A. Panov *et al.*, Bull. Russ. Acad. Sci. Phys. **71**, 494 (2007).
[9] M. Amenomori *et al.*, Adv. Space Res. **47**, 629 (2011).
[10] T. Antoni *et al.*, Astropart. Phys. **24**, 1 (2005); W. D. Apel *et al.* Astropart. Phys. **31**, 86 (2009); **47**, 54 (2013).
[11] J. R. Hörandel, Mod. Phys. Lett. A **22**, 1533 (2007).
[12] M. A. K. Glasmacher *et al.*, Astropart. Phys. **12**, 1 (1999).
[13] G. Aielli *et al.*, Nucl. Instrum. Methods Phys. Res., Sect. A **562**, 92 (2006).
[14] B. Bartoli *et al.*, Phys. Rev. D **84**, 022003 (2011).
[15] B. Bartoli *et al.*, Phys. Rev. D **85**, 092005 (2012).
[16] B. Bartoli *et al.*, Phys. Rev. D **91**, 112017 (2015).
[17] S. S. Zhang *et al.*, Nucl. Instrum. Methods Phys. Res., Sect. A **629**, 57 (2011).
[18] B. Bartoli *et al.*, Chin. Phys. C **38**, 045001 (2014).
[19] Z. Cao *et al.*, Chin. Phys. C **34**, 249 (2010).
[20] H. H. He *et al.*, LHAASO Project: Detector design and prototype, in *Proceedings of the 31st International Cosmic Ray Conference, ŁÓDŹ, 2009*, http://icrc2009.uni.lodz.pl/proc/pdf/icrc0654.pdf.
[21] XP3062 PMT data sheet, http://www.hzcphotonics.com/products/XP3062.pdf.
[22] G. Aielli *et al.*, Nucl. Instrum. Methods Phys. Res., Sect. A **608**, 246 (2009).
[23] M. Iacovacci, T. Di Girolamo, G. Di Sciascio, S. Mastroianni, and L. Saggese, Nucl. Phys. B, Proc. Suppl. **136**, 376 (2004).
[24] B. Bartoli *et al.*, Astropart. Phys. **67**, 47 (2015).
[25] B. Bartoli *et al.*, Nucl. Instrum. Methods Phys. Res., Sect. A **783**, 68 (2015).
[26] I. De Mitri *et al.* (ARGO-YBJ Collaboration), Nucl. Instrum. Methods Phys. Res., Sect. A **742**, 2 (2014).
[27] L. L. Ma *et al.*, The monitoring of weather and atmospheric condition of LHAASO site, in *Proceedings of the 32nd International Cosmic Ray Conference, Beijing, 2011*, http://www.ihep.ac.cn/english/conference/icrc2011/paper/proc/vb/vb_1033.pdf.
[28] G. Di Sciascio *et al.*, arXiv:0710.1945.
[29] D. Heck, J. Knapp, J. Capdevielle, G. Schatz, and T. Karlsruhe-Wissenhaltliche Berichte, Report No. FZKA 6019, Forschungszentrum, 1998.
[30] S. Ostapchenko, Nucl. Phys. B, Proc. Suppl. **151**, 143 (2006).
[31] H. Fesefeldt, Report No. PITHA 85-02, RWTH Aachen, 1985.
[32] Guo Yi-Qing *et al.*, Chin. Phys. C **34**, 555 (2010).
[33] J. L. Liu *et al.*, J. Phys. G **36**, 075201 (2009).
[34] J. R. Hörandel, Astropart. Phys. **19**, 193 (2003).
[35] M. Amenomori *et al.*, Phys. Rev. D **62**, 112002 (2000); Astrophys. J. **678**, 1165 (2008).
[36] T. K. Gaisser *et al.*, Astropart. Phys. **35**, 801 (2012).
[37] A. M. Hillas, Cerenkov light images of EAS produced by primary gamma rays and by nuclei, in *Proceedings of the 19th International Cosmic Ray Conference, La Jolla, 1985*, http://ntrs.nasa.gov/archive/nasa/casi.ntrs.nasa.gov/19850026666.pdf.

[38] M. Cardillo, E. Amato, and P. Blasi, Astropart. Phys. **69**, 1 (2015).
[39] G. D' Agostini, Nucl. Instrum. Methods Phys. Res., Sect. A **362**, 487 (1995).
[40] E.-J. Ahn, R. Engel, T. K. Gaisser, P. Lipari, and T. Stanev, Phys. Rev. D **80**, 094003 (2009).
[41] G. Battistoni *et al.*, The FLUKA code: Description and benchmarking, in *Proceedings of the Hadronic Shower Simulation Workshop 2006*, vol. 896, edited by M. Albrow and R. Raja (AIP, 2007), p. 31; A. Fass *et al.*, FLUKA: A multi-particle transport code, Technical Report No. CERN-2005-10, No. INFN/TC05/11, No. SLAC-R-773, SLAC, 2005.
[42] H. Menjo *et al.*, Nucl. Instrum. Methods Phys. Res., Sect. A **692**, 224 (2012).
[43] M. Ambrosio *et al.*, Phys. Rev. D **56**, 1418 (1997).
[44] P. O. Lagage and C. J. Cesarsky, Astron. Astrophys. **125**, 249 (1983).
[45] E. G. Berezhko, L. T. Ksenofontov, and H. J. Volk, Astron. Astrophys. **505**, 169 (2009).
[46] K. Kobayakawa, Y. Sato, and T. SamuraPhys. Rev. D **66**, 083004 (2002).
[47] P. L. Biermann, arXiv:astro-ph/9501030.
[48] J. R. Jokipii and G. Morfill, Astrophys. J. **312**, 170 (1987).